PNAS
www.pnas.org

Supplementary Information for

Bipolar Switching by HCN Voltage Sensor Underlies Hyperpolarization Activation.

John Cowgill, Vadim A. Klenchin, Claudia Alvarez-Baron, Debanjan Tewari, Alexander Blair, and Baron Chanda

Baron Chanda
Email: chanda@wisc.edu

This PDF file includes:

Figs. S1 to S7
Tables S1

SUPPLEMENTARY FIGURE LEGENDS

Fig. S1. Sequence alignment of voltage-gated ion channels from CNBD family
Sequence alignment of the transmembrane segments of some well-studied voltage-gated channels in the CNBD family from mammals (human HCN1, mouse HCN2, rat EAG1, human hERG), invertebrates (sea urchin spHCN) and plants (tomato LKT1, arabidopsis KAT1 and SKOR). The channels activated by hyperpolarization are shown in red and those activated by depolarization are in black. The sequences were first aligned by T-Coffee Expresso and then manually adjusted to match experimentally determined structures of hHCN1, rEAG1 and hERG (PDB entries 5U6O, 5K7L and 5VA1). Helical structures of hHCN1 are indicated by purple ribbons. The coloring scheme used divides residues into five groups: charged acidic, charged basic, hydrophobic/non-polar, uncharged polar and prolines. Arrows and numbers indicate different junction points for the chimeric channels as indicated in the text with the primary junction points used throughout the paper highlighted in red.

Fig. S2. Initial chimeras tested
(A-C) Preliminary scanning for functional chimeras between hEAG1 and spHCN (A), mHCN1 (B), and mHCN2 (C). Cartoon representation of the constructs that did not display detectable currents are shown on the left. Numbers below each cartoon correspond to the junction points used for generating each construct according to the numbering in Fig. S1. Functional constructs are shown on the right together with representative traces from two-electrode voltage clamp (for constructs in A) or cut-open voltage clamp (for constructs in B) and G-V curves with errors representing SEM for n=3 (for constructs in A) or 4 (for constructs in B).

Fig. S3. Observed currents pass through the central pore of the injected construct.
(A-B) Example recordings from uninjected oocytes (A) compared to currents from the HHHEH and EEHEH constructs (B). Test pulses from the shown holding potential ranged from -150 mV up to 60 mV and are shown every 20 mV. Note that the currents in uninjected oocytes have been scaled up on the Y-axis to show features more clearly. (C) Current-voltage relationships for uninjected oocytes compared to the HHHEH and EEHEH chimeras. Error bars show SEM for n=5 (for uninjected and HHHEH) or 4 (for EEHEH) (D) Example data of modification of EAG A470C and HHHEH A470C by 5 mM MTSEA. For the first 3 pulses, solution was exchanged with fresh external solution (100 mM K/5 mM Na) to ensure no run down or potassium accumulation was occurring. Prior to the fourth pulse, solution was exchanged with external solution containing 5 mM MTSEA. Normal external solution without MTSEA was exchanged prior to the final recording to ensure the reduction in current amplitude persisted washout of MTSEA. There was a 30 second incubation at the holding potential between each pulse while solutions were exchanged. (E-F) Time course and reversibility of modification of hEAG-A470C (E) and HHHEH-A470C (F). Pulses to +60 mV (E) or -150 mV (F) were repeated every 20 seconds and normalized to the maximum observed current. Solution was exchanged for external solution containing 5 mM MTSEA or 10 mM DTT following the indicated data point. The MTSEA was washed out prior to application of DTT using external solution. (G) Modification by MTSEA is blocked by co-application with DTT for the HHHEHA470C construct. The experimental procedure was the same as in (F) except that 5 mM MTSEA was first added in the presence of 10 mM DTT. MTSEA was then applied alone to ensure the observed currents were responsive to MTSEA under non-reducing conditions. These experiments rule out the possibility that the observed block is due to quaternary ammonium ion rather than MTS modification of substituted cysteines.

Fig. S4. Activation kinetics in the HHHE*H construct.
(A) Three gating schemes observed in voltage-gated ion channels. Non-inactivating channels (black trace) show residual currents following return to negative potentials because the channel does not close immediately and are referred to as "tail" currents. The peak tail current observed for a non-inactivating channel occurs immediately at the onset of the repolarizing pulse. When the channel inactivates with a rate similar to the activation process (cyan trace), the tail current rises to a peak in a "hooked" shape and the peak current amplitude upon depolarization and repolarization are equal (due to symmetry of pulse amplitude and reversal of 0 mV). Finally, when the rates of inactivation/recovery from inactivation are 10 times faster than activation/deactivation (orange trace), virtually no current is observed upon depolarization, but repolarization is accompanied by large hooked tail currents. These are classically referred to as resurgent currents. Scales for all traces are identical and the charge for each transition was fixed at 1 e^-. The parameters α and β correspond to an intrinsic rate of 1 s^{-1}. (B) Envelope of tails protocol under symmetric solutions (100 mM $K^+_{internal}$/100 mM $K^+_{external}$) in cut-open voltage clamp showing the growth of tail currents elicited by depolarizing pulses of increasing length to 20 mV or 40 mV (reproduced from Fig. 3D for comparison). (C) Conductance plotted as a function of time at steady-state (filled circles) or peak tail (open circles) from depolarizing pulses to 20 mV (blue) or 40 mV (red). (D) Three-pulse protocol on the HHHE*E chimera in symmetrical solutions. Note that a P1 pulse of 3 seconds was used from a holding potential of -90 mV and only the final 10 ms is shown for clarity. (E) Three-pulse protocol using a similar protocol as in (D) using either 100 mM Na^+/5 mM K^+ (black) or 100 mM TEA^+/5 mM K^+ external solution. Time constants of a fit to monoexponential decay of the P3 pulse current are shown.

Fig. S5. HCN1 is minimally affected by the removal of its C-terminus
(A) Cartoon representation, sequence, and representative current traces for the C-terminal deletion of mHCN1 fused to mCherry. (B) G-V curves for the wild type mHCN1 fused to mCherry and its C-terminal deletion construct depicted in (A). Experimental conditions were identical to those used to generate data show in Figure 1. Error bars represent SEM for n=5.

Fig. S6. Residues near the channel gate influence the stability of depolarization-dependent opening.
(A) Sequences of HHHE*H variants (HHHE*H2 to HHHE*H5) that contain increasingly larger HCN1-derived contribution to S5 and the S6/C-linker region of EAG1 pore. (B) Cartoonsand representative COVG currents for the chimeras with EAG1/HCN1 junction points shown in (A). The inset for HHHE*H2 data clearly shows a lack of resurgent currents. Scale bars denote 2 μA (vertical) and 500 ms (horizontal). (C) G-V curves for the new mosaics with error bars showing SEM for n= 3 (HHHE*H4) or 4 (all others). Compare to the parent construct in Figure 3C. (D) Cartoon representation, sequence, and representative current traces for the C-terminal deletion mosaic that contains last eight HCN1-specific residues immediately following the gating glutamine residue. (E) Comparison of the G-V curves between the original truncation construct and its HHHE*ΔC2 variant depicted in (A).

Fig.S7. Fits of HCN1 and EAG to the universal gating scheme
Left: Cartoon representations and models the HCN1 and hEAG parent constructs used in this study. Middle: Simulated currents traces from the model in response to the same pulse protocol applied in the electrophysiological recordings for both constructs. Parameters for simulations can be found in Table S1. Right: Probability vs. voltage

curves for each state in the model measured as the probability of occupancy of each state over the final 10 ms of each test pulse. Probability curves are colored according to the models with the hyperpolarized open state in red, closed state in blue, depolarized open state in black, and inactivated state in gray.

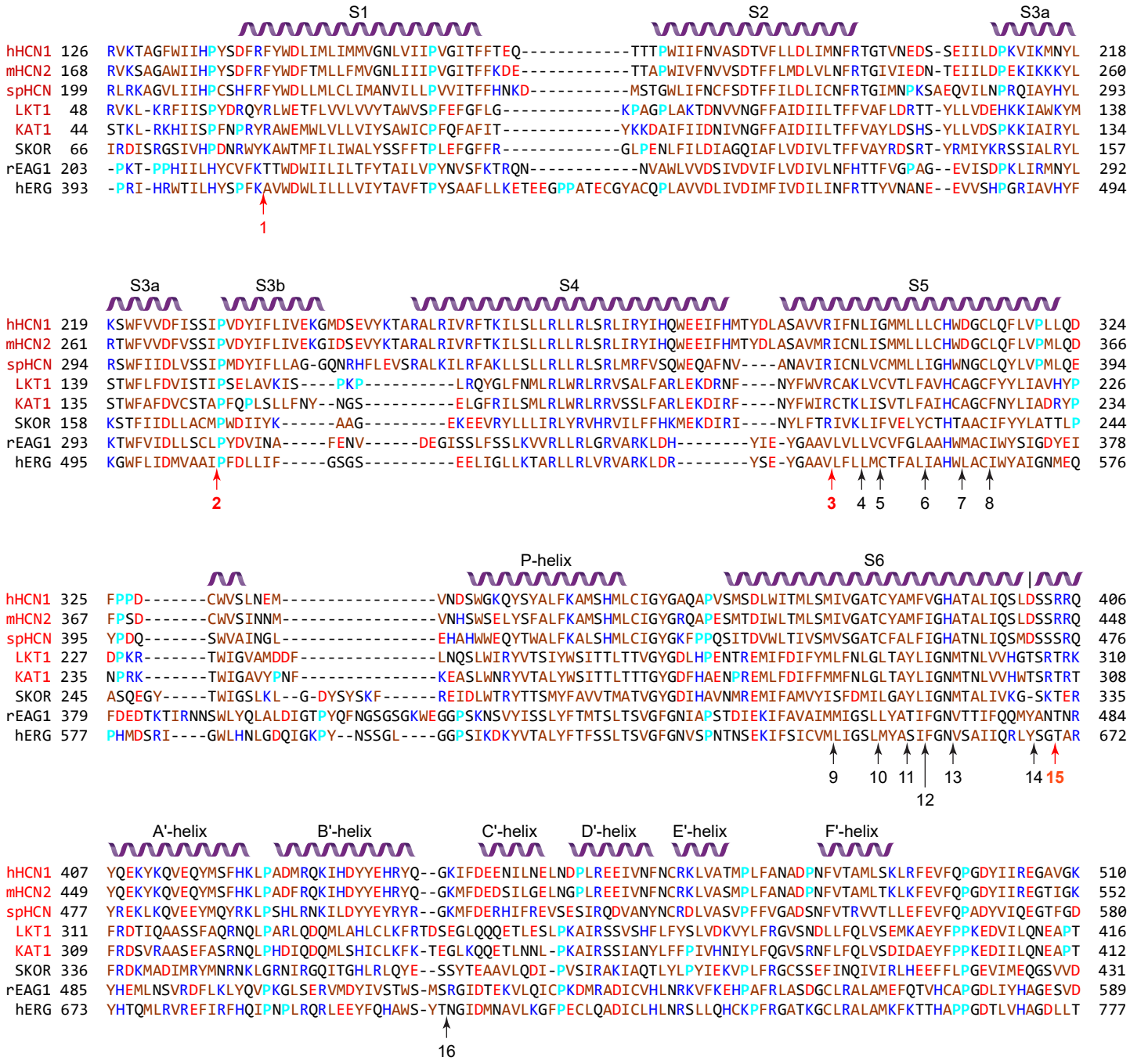

Figure S1 Cowgill et al. 2018

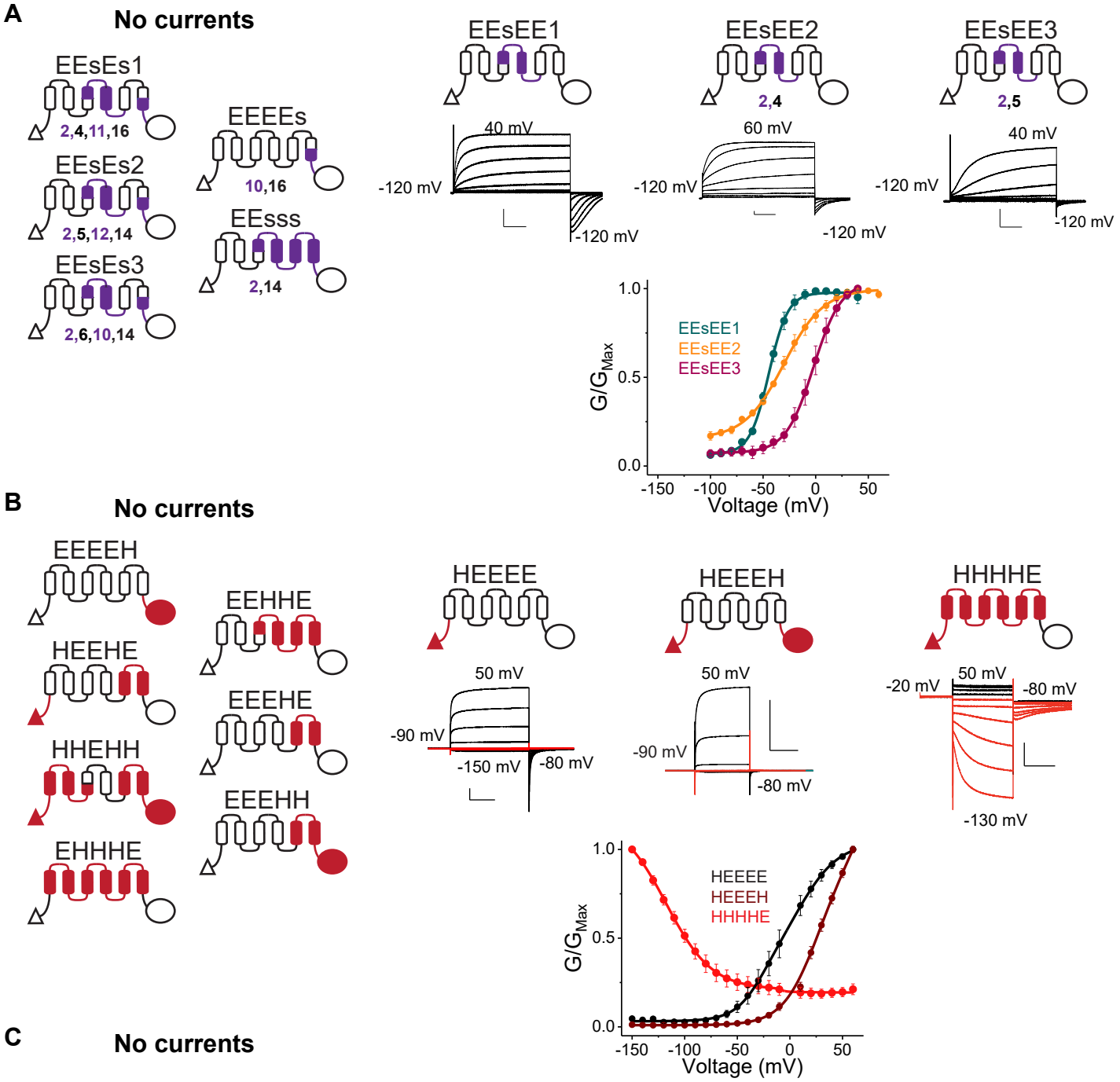

Figure S2 Cowgill et al. 2018

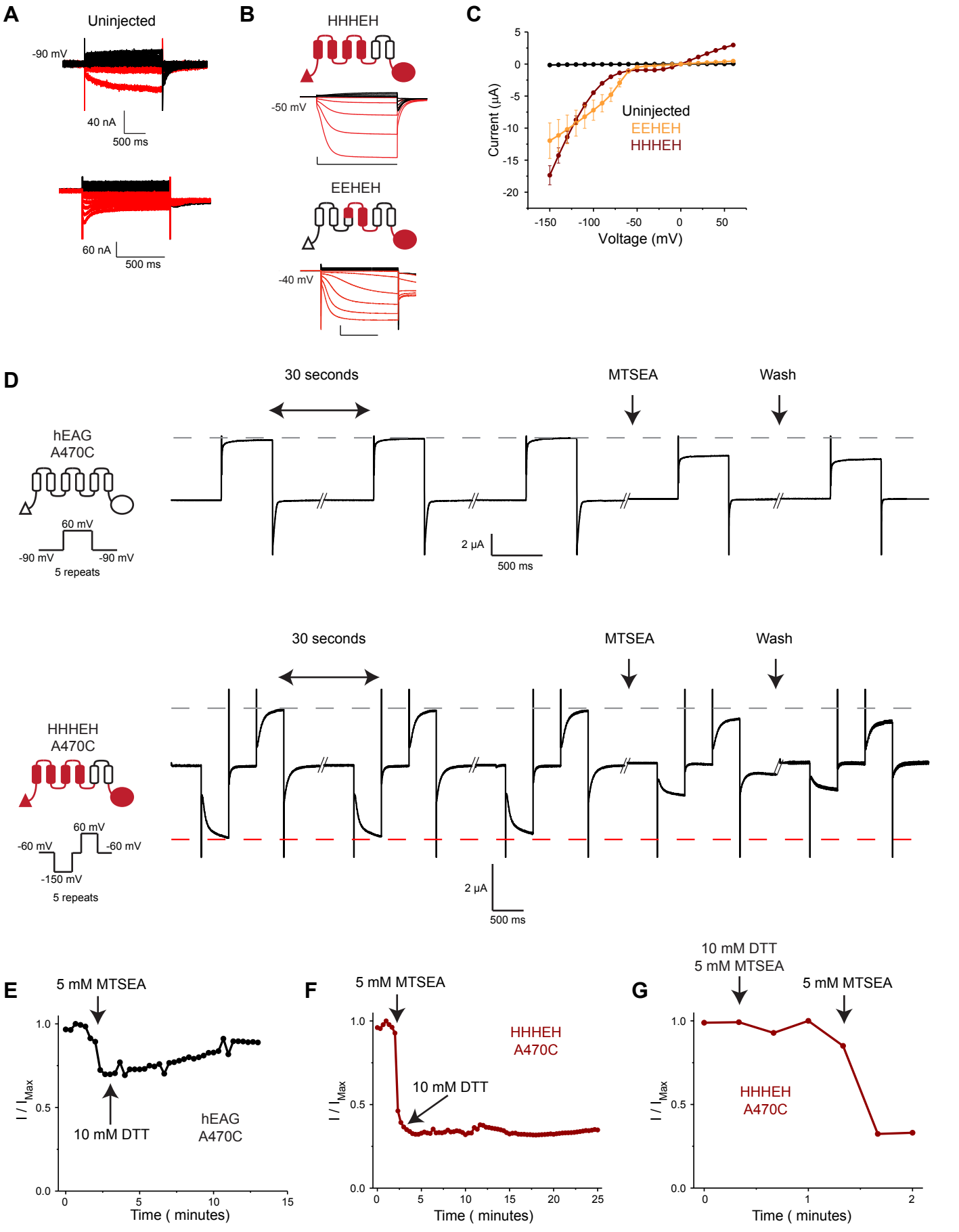

Figure S3 Cowgill et al. 2018

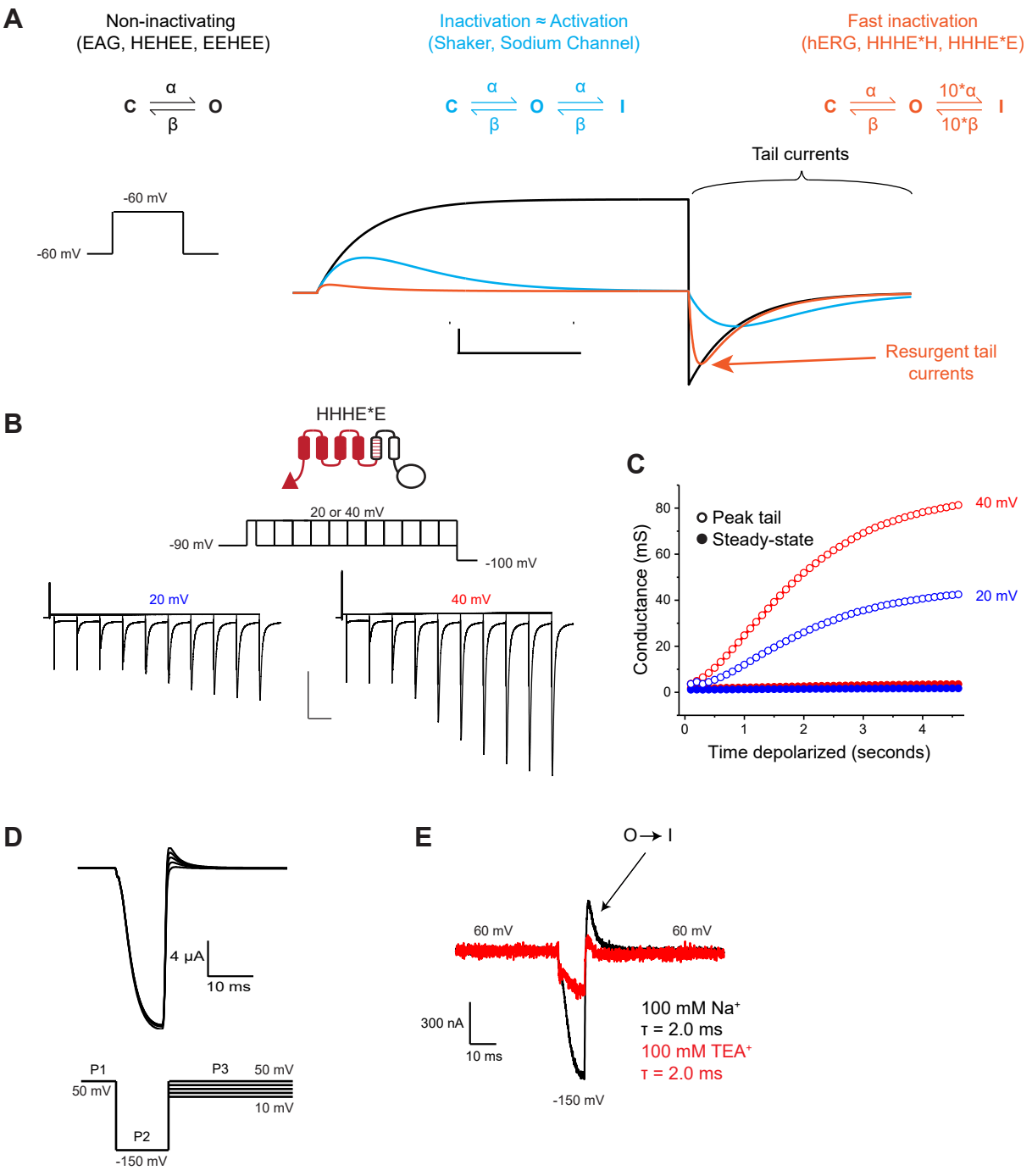

Figure S4 Cowgill et al. 2018

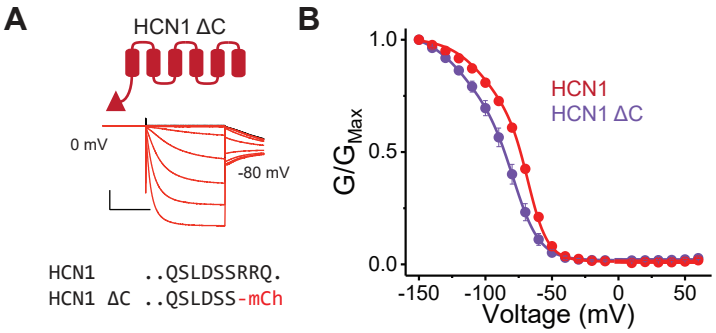

Figure S5 Cowgill et al. 2018

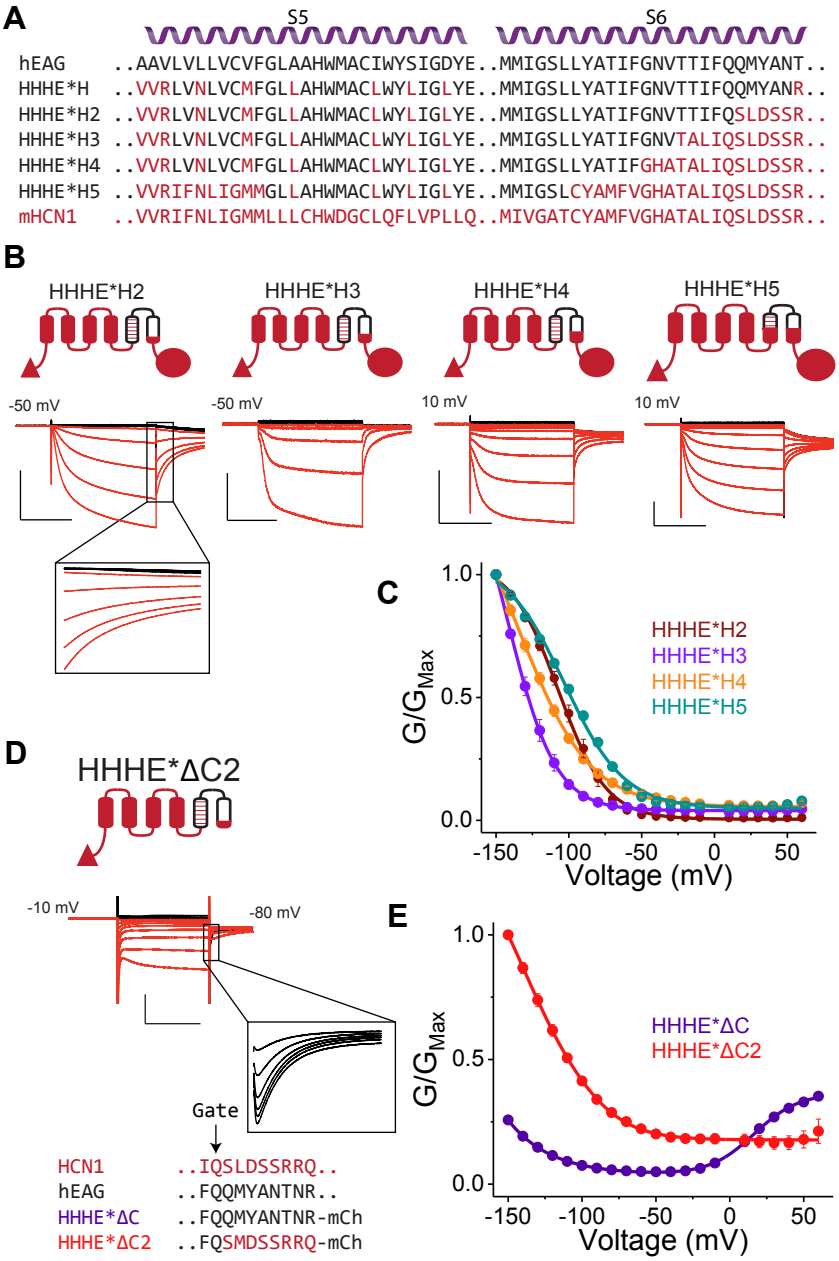

Figure S6 Cowgill et al. 2018

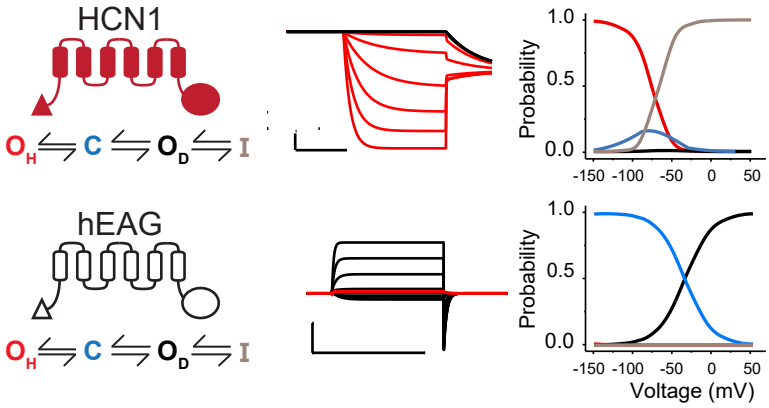

Figure S7 Cowgill et al. 2018

Construct	Transition	Rate (s^{-1})	Charge (e^-)
HHHEH	O_H to C	267	0.74
	C to O_H	0.314	-0.70
	C to O_D	0.725	0.19
	O_D to C	0.745	-1.1
HHHE*H	O_H to C	522	1.0
	C to O_H	$8.76x10^{-3}$	-1.2
	C to O_D	0.366	0.93
	O_D to C	0.353	-2.0
	O_D to I	147	1.0
	I to O_D	9.49	-0.36
HHHE*ΔC	O_H to C	181	0.36
	C to O_H	3.19	-0.013
	C to O_D	0.440	0.48
	O_D to C	1.30	-0.96
	O_D to I	5.83	0.97
	I to O_D	144	-0.49
HHHE*ΔC-SD	O_H to C	119	0.33
	C to O_H	1.69	-0.52
	C to O_D	10.6	0.83
	O_D to C	35.9	$-7.1x10^{-6}$
	O_D to I	984	$4.8x10^{-4}$
	I to O_D	299	-0.78
HCN1	O_H to C	409	0.49
	C to O_H	29	-0.73
	C to O_D	12.6	0.25
	O_D to C	25.1	-0.72
	O_D to I	614	0.40
	I to O_D	1.00	-0.47
hEAG	O_H to C	251	0.28
	C to O_H	$1.3 x10^{-4}$	-1.4
	C to O_D	36.3	0.70
	O_D to C	4.63	-0.79
	O_D to I	$1.9 x10^{-3}$	0.28
	I to O_D	87.5	-0.31

Table S1 Parameters for kinetic models used in simulations